

**Weakening of cold halocline layer exposes sea ice to oceanic heat in the eastern Arctic Ocean**

Polyakov, Igor ; Rippeth, Tom; Fer, Ilker; Alkire, Matthew; Baumann, Till; Carmack, Eddy; Ivanov, Vladimir; Janout, M.A.; Padman, Laurie; Pnyushkov, Andrey; Rember, Robert

Journal of Climate

DOI:
[10.1175/JCLI-D-19-0976.1](https://doi.org/10.1175/JCLI-D-19-0976.1)

Published: 15/09/2020

Publisher's PDF, also known as Version of record

[Cyswllt i'r cyhoeddiad / Link to publication](#)

Dyfyniad o'r fersiwn a gyhoeddwyd / Citation for published version (APA):

Polyakov, I., Rippeth, T., Fer, I., Alkire, M., Baumann, T., Carmack, E., Ivanov, V., Janout, M. A., Padman, L., Pnyushkov, A., & Rember, R. (2020). Weakening of cold halocline layer exposes sea ice to oceanic heat in the eastern Arctic Ocean. *Journal of Climate*, 33(18), 8107-8123. <https://doi.org/10.1175/JCLI-D-19-0976.1>

Hawliau Cyffredinol / General rights

Copyright and moral rights for the publications made accessible in the public portal are retained by the authors and/or other copyright owners and it is a condition of accessing publications that users recognise and abide by the legal requirements associated with these rights.

- Users may download and print one copy of any publication from the public portal for the purpose of private study or research.
- You may not further distribute the material or use it for any profit-making activity or commercial gain
- You may freely distribute the URL identifying the publication in the public portal ?

Take down policy

If you believe that this document breaches copyright please contact us providing details, and we will remove access to the work immediately and investigate your claim.

63 **1. Introduction**

64 In recent decades there has been a dramatic decline in seasonal sea ice extent in the Arctic
65 Ocean, with a more recent year-around decline in sea ice extent, area and volume (Kwok 2018;
66 Stroeve and Notz 2018). This change has shifted the local radiative balance resulting in a
67 positive ice-albedo feedback mechanism as increasing lead fraction and surface melt pond areas
68 in decaying Arctic sea ice facilitate enhanced upper-ocean solar heating and more rapid melting
69 of ice floes (e.g., Perovich et al. 2008; Toole et al. 2010). Moreover, it was hypothesized that the
70 declining sea ice has larger scale hemispheric impacts on the North Atlantic Oscillation and, in
71 consequence, mid-latitude weather patterns (e.g., Francis et al. 2017; Garcia-Serrano et al. 2015;
72 Kolstad and Screen 2019).

73 Heat associated with oceanic currents originating from lower latitudes provides an important,
74 and year-round, source of heat to the Arctic Ocean (e.g., Carmack et al. 2015). The dominant
75 external source of oceanic heat is the warm (temperature $>0^{\circ}\text{C}$) and salty water of Atlantic origin
76 (Atlantic Water, AW) which is distributed throughout the deep basins at intermediate depths
77 (~150-900 m, **Fig. 1**) and holds sufficient heat to melt the Arctic sea ice 3-4 times over (Carmack
78 et al. 2015). Across much of the eastern ($>70^{\circ}\text{E}$) Eurasian Basin (EB) this heat is isolated from
79 the surface, and hence the sea ice, by large vertical density gradients associated with the Arctic
80 halocline (60-150 m, **Fig. 1**). The presence of the halocline impedes the transport of AW heat
81 upward towards the surface across much of the Arctic Ocean (e.g., Fer 2009). The exception to
82 this is the western ($<70^{\circ}\text{E}$) Nansen Basin where substantial turbulent mixing linked to the tides
83 (Fer et al. 2010; Padman and Dillion 1991; Rippeth et al. 2015; Renner et al. 2019) and wind
84 events (e.g. Provost et al., 2017; Graham et al., 2019) supports heat fluxes in excess of 50 W m^{-2}

85 Inflowing AW is warming (Barton et al. 2018) driving a regime shift in sea ice cover over the
86 past decade in the Barents Sea (Onarheim et al. 2018). There is also a growing body of evidence
87 that the characteristics of the Arctic halocline are changing; for example, the halocline has
88 weakened in the eastern EB since the 1970s (Steele and Boyd 1998; Polyakov et al. 2010). These
89 changes have accelerated over the past decade (Polyakov et al. 2020a) with continuous time
90 series from moored instruments capturing the significant weakening of the cold halocline layer
91 (the upper part of the halocline with temperatures near freezing and negligible vertical
92 temperature gradient) and shoaling of the AW in 2013-2015 (Polyakov et al. 2017).

93 The combination of weaker stratification and shoaling of the AW in the EB, coupled with the
94 loss of sea ice, has allowed progressively deeper winter ventilation in the eastern EB in recent
95 years (Polyakov et al. 2017). This process further enhances the annually averaged upward AW
96 heat fluxes. The shift in sea ice state and upper ocean stratification to conditions previously
97 unique to the western Nansen Basin has been termed ‘atlantification’ (Polyakov et al. 2017) and
98 represents a transition toward a new Arctic climate state, in which the geographical influence of
99 the AW heat on sea ice volume is spreading eastwards.

100 Since the increased oceanic heat fluxes associated with atlantification drive sea ice melt, and
101 reduced sea ice increases oceanic heat fluxes through increased convective entrainment in
102 winter, this process represents a positive ice/ocean-heat feedback mechanism. This mechanism is
103 analogous and complementary to the ice-albedo feedback, in which atmospheric warming leads
104 to a reduction of ice and snow coverage and decreasing albedo, resulting in further snow and sea
105 ice retreat (Manabe and Stouffer 1980).

106 The strength of the ice/ocean-heat feedback is determined by the vertical flux of AW heat
107 across the halocline into the surface-forced seasonal convective layer. Polyakov et al. (2017)

108 estimated seasonal changes of heat content Q in the eastern EB halocline (65-130 m) and an
109 equivalent divergent heat flux (the difference of fluxes at two depth levels for which a 1D
110 equation of heat balance for a unit-area water column is integrated) of $\delta F_h \sim 12 \text{ W m}^{-2}$ over this
111 depth range for winter 2013-2014, and $\sim 8 \text{ W m}^{-2}$ for winter 2014-2015. They argued that these
112 inferred values of δF_h exceeded previous regional estimates (e.g., Lenn et al. 2009; Polyakov et
113 al. 2013) by a factor of 2-4 and potentially account for an additional loss of up to 18-40 cm of
114 sea ice over this period of time associated with the increase in upward AW heat transport. In
115 consequence the impact of the oceanic heat flux on sea ice formation in 2013-2015 was
116 comparable to that of the atmospheric thermodynamic forcing (Polyakov et al. 2017).

117 The aim of this paper is to quantify the changes in the upper ocean heat content, and the
118 consequent release of heat from the AW up into the halocline and to the surface mixed layer in the
119 key eastern Eurasian Basin of the Arctic Ocean. We improve on the Polyakov et al. (2017) study
120 by including new data collected over the period 2015-2018 to quantify changes in the upper ocean
121 heat content, and the consequent release of heat from the AW up into the halocline and to the
122 surface mixed layer in the EB. We then compare these regional estimates with earlier estimates.

123 **2. Data**

124 Our analyses utilize observations of ocean temperature, salinity, and currents from moorings
125 deployed in the eastern EB (**Fig. 2, Table 1**). Observations at the M1₄ mooring site began in
126 August 2002, with several co-located moorings deployed and recovered annually prior to 2009,
127 and longer duration of deployments since 2013 (**Table 1**).

128 Moorings deployed in summer 2013 and recovered in summer 2015 provided two-year long
129 records for most instruments except for the M1₅ upper ocean Acoustic Doppler Current Profiler
130 (ADCP), which worked for 10 months only. Mooring M3 located off Severnaya Zemlya, was

131 deployed at water depth of 1350 m. Six moorings (M1₁-M1₆) formed a ~350-km cross-slope
132 section spanning from the 250 m to 3400 m isobaths along 126°E. Topographically steered
133 boundary current flows along slope across this section (Pnyushkov et al. 2015, 2018). Averaged
134 over 2013-2015, the maximum current speed of ~11 cm/s was found at the shallowest mooring
135 M1₁ (on the 250 m isobath), with only ~0.5 cm/s in the deep basin at moorings M1₅ and M1₆.
136 The AW core defined by the maximum water temperature is typically located at the M1₅
137 mooring site at a depth of ~250 m.

138 Deployment of moorings in 2015-2018 repeated the mooring distribution used for 2013-2015
139 except that the M1₆ mooring was not re-deployed (**Table 1**). Almost all mooring instruments
140 provided full three-year long records; the M1₃ McLane Moored Profiler (MMP) stopped
141 recording after two years. In addition, a short-term mooring, M1_{4-short}, was deployed for 18 days
142 only (September 2–20, 2018) close to the M1₄ climatologic mooring site (**Table 1**). The short-
143 term mooring was designed to provide current and CTD data with the most rapid possible
144 sampling rate in the upper 200 m.

145 *Mooring Conductivity-Temperature-Depth (CTD) data:* The MMP-based moorings at the M1₄
146 mooring location in 2002-2009 collected temperature, salinity and current velocity profiles once
147 per day. Four 2013-2015 moorings (M1₂, M1₃, M1₅, and M1₆) and two 2015-2018 moorings
148 (M1₃ and M1₅) provided vertical MMP profiles with two-day sampling interval with a ~0.25 m
149 spacing. The MMPs on most moorings sampled the 50–700 m depth range; however, the 2015-
150 2018 M1₅ mooring missed its target depth and the MMP record only reached to ~170 m below
151 the surface. The MMP on the M1_{4-short} mooring sampled about every 18 minutes and obtained
152 1369 profiles. The MMP temperature and conductivity calibrated measurement accuracies are
153 ±0.002°C and ±0.002 mS/cm.

154 The moorings M1₁, M1₂, M1₄ and M3 with no MMP profilers deployed in 2013–2018, as
155 well as mooring M1g, deployed about 12 km from mooring M1₄ in 2008 –2010 (**Fig. 2, Table 1**)
156 were equipped with Seabird SBE-37 CTD instruments and provided records of conductivity,
157 temperature and pressure with sampling interval of one hour or shorter, with measurement
158 accuracies for temperature and conductivity of $\pm 0.002^{\circ}\text{C}$ and $\pm 0.003\text{ mS/cm}$, respectively.

159 *Mooring current data:* Most moorings used in this analysis included 300 kHz Acoustic
160 Doppler Current Profilers (ADCP) targeting the upper 50-60 m of the water column (**Table 1**).
161 Moorings with no MMP were also equipped by long-range ADCP 75 kHz covering deeper layers
162 (**Table 1**). ADCPs provided current velocities, averaged over 2-m (prior to 2013) or 4-m (after
163 2013) vertical cells, with 1-h time resolution. The manufacturer's estimates for ADCP accuracies
164 are 0.5% of measured speed and 2° for current direction.

165 Moorings equipped with MMPs provided current velocity profiles with above mentioned
166 profiling intervals and 0.25 m vertical resolution. The MMPs were equipped with a Falmouth
167 Scientific Inc. (FSI) micro-CTD sensor in 2002-2004 and a Sea-Bird Electronics (SBE) 41CP
168 CTD sensor starting from 2004, with temperature and conductivity measurement accuracies of
169 about $\pm 0.002^{\circ}\text{C}$ and $\pm 0.0003\text{ S/m}$, respectively. Prior to 2013, the MMPs carried the FSI
170 Acoustic Current Meters (ACM); after 2013, the ACMs were substituted with the FSI ACM-
171 PLUS-MP (<http://www.falmouth.com/product-information.html>). The velocity precision of the
172 FSI ACM (ACM-PLUS-MP) carried on the MMP are reported to be $\pm 2\%$ (1%) of reading and
173 $\pm 0.5\text{ cm/s}$ for velocity resolution. Compass accuracy is $\pm 2^{\circ}$. All MMP sensors were calibrated
174 before their deployment and immediately after their recovery using McLane facilities.

175 *Ship-borne CTD data:* Mooring observations were complemented by repeated hydrographic
176 profiles collected using a Seabird SBE911plus CTD system in 2013, 2015 and 2018 at M1₄

177 mooring site (**Fig. 2**). The effective vertical resolution, considering the different sensor
178 characteristics, is about 25 cm. Individual temperature and conductivity measurements are
179 accurate to $\pm 0.002^\circ\text{C}$ and $\pm 0.0003\text{ S/m}$.

180 **3. Methods**

181 *Defining a proxy for Richardson (Ri) number:* Ri is a measure of the stability of the water
182 column, *ie.* when $Ri < 0.25$ the vertical shear in the flow is sufficient to generate instability and
183 turbulent mixing. As such Ri estimates provide a useful indicator for the likelihood of shear
184 instability/ mixing. The correct scale for the estimation of Ri is the Ozmidov scale (which in this
185 case we estimate to be $O(0.1\text{m})$). However, the vertical resolution of the Ri estimate is limited by
186 the positions of instruments on the moorings which have a vertical resolution of 20m. Whilst the
187 20 m Ri estimates are likely to smooth out the fine structure of individual instabilities, we argue
188 that the smaller the large-scale Ri value is, the greater the likelihood of shear instability (and so
189 turbulence and mixing). As such the 20m Ri provides a useful proxy for the likelihood of shear
190 instability. Moreover, trends in the 20m (proxy) Ri estimate will expose trends in the likelihood
191 of shear instability, the key interpretation here. This approach is supported by direct comparisons
192 of dissipation and low resolution Ri estimates (e.g. Mead Silvester et al., 2014).

193 The mooring-based estimates of Ri (**Fig. 5**) are based on MMP measurements of stratification
194 and velocity. Stratification over the 100-140 m layer is quantified using buoyancy frequency (N),
195 $N^2 = -(g/\rho_o)\partial\rho/\partial z$, where ρ is the potential density of seawater, ρ_o is the reference density (1030
196 kg m^{-3}), and g is the acceleration due to gravity. The limited depth range of 100-140m was
197 chosen due to insufficient data coverage in early years (see **Table 1**). The Ri proxy was
198 estimated as $Ri = N^2/|\mathbf{U}_z|^2$, where $|\mathbf{U}_z|$ is the magnitude of the vertical shear of the horizontal

199 currents; $|\mathbf{U}_z|$ and N were calculated averaging gradients over 20 m vertical scale for all points
200 within the 100-140 m depth range.

201 *Defining timing and depth of seasonal upper ocean ventilation and divergent heat flux δF_h :*

202 For this analysis, temperature observations carried out by M1₂, M1₃, M1₄ and M3 moorings in
203 2013–2018 were used. SBE-37 data from non-MMP moorings M1₂ (2015–2018), M1₃, M1₄ and
204 M3 were complemented by MMP profiles from M1₂ (2013–2015) mooring. SBE-37
205 observations were linearly interpolated to match the MMP vertical resolution. We are interested
206 in the analysis of seasonal ventilation of the halocline. Accordingly, temperature observations
207 were filtered using wavelet transformations to keep seasonal variations only (and thus different
208 temporal sampling by MMP and SBE-37 did not affect our results). A standard package of
209 wavelet programs was used based on the DOG Mother function. Estimates of heat content (Q ,
210 J/m^3 , with freezing point taken as a reference temperature at a given salinity) for the halocline
211 (65-140 m) are shown in **Fig. 6**. To assure that the use of SBE-37 point measurements with
212 relatively coarse vertical resolution and continuous MMP profiles for estimates of Q did not
213 affect our results we calculated Q using MMP temperature record from M1₂ mooring (2015–
214 2018) twice, first time with original MMP resolution and another one with sub-sampled coarser
215 resolution matching SBE-37 depth levels (**Table 1**). Results of Q integrated over the halocline
216 depth range and averaged in time over the entire record length differed by 8%.

217 The aim is to define the timing and amplitude of upward heat flux associated with winter
218 ventilation. To this end, we identified timing and amplitude of the maximum Q (as accumulated
219 over the warm phase of the seasonal cycle) and the minimum of Q (associated with winter
220 ventilation) using Q vertically integrated over 65-140 m. The depth of the ventilation is defined

221 as the deepest point where a distinct minimum of Q was found. The maximum of vertically
222 integrated Q was then re-calculated using the depth of ventilation.

223 Following Polyakov et al. (2017), we limited the boundary of the winter ventilation layer to
224 140 m. For some years, the boundary of the layer was deeper (as shown in **Fig. 6** by the black
225 horizontal segments located at the very bottom of the panels with Q). Therefore, our choice of
226 the ventilation layer is conservative and estimates of divergent heat fluxes δF_h derived from
227 change of heat content ΔQ during each winter season represent the lower bound, consistent with
228 the objectives of the study. For the upper boundary of the layer for which Q is estimated, we
229 selected the depth 65 m, chosen because this best determines the halocline layer in which heat
230 from the AW is stored and released (Polyakov et al. 2013, 2017). We evaluated the sensitivity of
231 our estimates to the choice of the boundary of the ventilation layer by calculating δF_h for 65-140
232 m and 65-150 m layers. The 10 m increase in layer thickness increases δF_h by less than 8%.

233 Following Polyakov et al. (2013), we estimated δF_h (W/m^2) between two depth levels as the
234 change, in time, of vertically integrated Q . This approach is based on the assumption that all
235 change in heat content is due to vertical exchange (so 1D). Note that these values are flux
236 *differences* between two depth levels, and total heat fluxes may be larger than these values due to
237 additional non-divergent heat transports; thus, our inferred estimates of divergent heat fluxes
238 represent *lower* bounds for the total heat flux (for details, see Polyakov et al. 2013).

239 **4. Results**

240 *a. AW warming and weakening of halocline stratification in the eastern Eurasian Basin*

241 Time series of the AW temperature show significant interannual variability (**Fig. 3a**). The AW in
242 the eastern EB began warming in the early 2010s, with the AW temperature in 2018 being, on

243 average, 0.5–0.7°C higher than in 2011 (**Fig. 3a**). This recent warming is particularly noticeable
244 at shallower depths, with the increase in temperature at 150 m exceeding 1.5°C between 2011
245 and 2018. This warming over the depth range 150-750 m between September 2013 – May 2014
246 and September 2016 – May 2017 is partially associated with shoaling of the upper halocline
247 boundary (**Fig. 3c**) and a substantial increase in AW layer thickness (**Fig. 4**).

248 Cross-correlation analysis of time series of AW temperature measured at 250m from 1997-
249 2018 in Fram Strait, the entry point of AW into the Arctic, and from 2002-2018 in the eastern EB
250 (red time series in **Fig. 3a**) shows the strongest correlation, $R = 0.67$, for a lag of 682 days (Fram
251 Strait series leads, **Fig. 3b**). The fit between the two time series is better over the last 7-8 years
252 than it is over the earlier period. The ~2 year lag suggests that warm pulses of AW that entered
253 the Arctic Ocean through Fram Strait, are traveling towards the eastern EB at a speed 2-2.5 times
254 faster than that estimated for a warm AW pulse which entered the eastern EB in 2004 (Polyakov
255 et al. 2005). This implies that the rate of advection has increased over time. However, noisy data
256 due to gaps in the EB record preclude meaningful statistical analysis using just the early part of
257 the time series. Assuming that the lagged correlation between the two time series will persist in
258 the near future, the latest part of the Fram Strait series (not shown) implies that the AW
259 temperature in the eastern EB reached its peak in late 2018 (these data are not yet available) and
260 will slowly decrease over the next 1-2 years.

261 Temperature and salinity profiles in the eastern EB from CTD during 2013-2018 and MMP
262 during 2003-2018 recorded a decline of stratification (N^2) over the 110-140m depth range of the
263 halocline (**Figs. 1c, 5a,b**) which may be a result of both the shoaling of AW and weakening of
264 halocline stratification. Polyakov et al. (2018) used available potential energy defined for the
265 variable-depth halocline to show overall weakening stratification in the EB since the 1980s, with

266 accelerated tendencies in the 2010s compared with the 2000s. However, the substantial
267 weakening of halocline stability from 2013 to 2015 (Polyakov et al. 2017) which continued in
268 2015–2018, and which was also partially associated with shoaling of the AW (**Fig. 4**) found at 80
269 m depth, as inferred from the most recent observations in winter 2017-2018 (**Figs. 3c**). This
270 represents the shallowest depth the AW has been observed in the 15 years of mooring
271 deployments. As these estimates used a linear interpolation of CTD time series made at 38m and
272 107m at mooring M1₄, we are not able to definitively conclude that the cold halocline layer was
273 present (albeit very thin) during the winter of 2017–2018. However, the record suggests the
274 extreme thinning (or even absence) of the Arctic cold halocline layer for several months at this
275 time (**Figs. 3c, 4**) implying that AW heat was exposed to winter convection associated with sea
276 ice formation and brine rejection.

277 *b. Increased oceanic heat fluxes and ice loss in the eastern Eurasian Basin*

278 The weakening stratification, shoaling of the AW layer and increase of current shear in recent
279 years (e.g., Polyakov et al. 2020b) have altered the seasonal cycle of upward AW heat transport
280 (**Fig. 6**). Estimated change in heat content (Q) from the halocline (65-140 m) during winter,
281 averaged at four moorings, is equivalent to mean divergent heat fluxes (Section 3) of
282 $\delta F_h = 12.0 \pm 5.5, 3.5 \pm 2.2, 3.0 \pm 1.9, 12.9 \pm 1.7$ and 20.6 ± 6.8 W/m² for five winters from 2013-2014
283 through 2017-2018 (**Figs. 6, 7**). For three of these winters (2013-2014, 2016-2017, and 2017-
284 2018), δF_h greatly exceeded (3- to 5-fold) the previous estimates derived from summer 2007-
285 2008 microstructure observations over the Laptev Sea slope (Lenn et al. 2009; Polyakov et al.
286 2019) and winter 2009-2010 ITP-37 observations in the central Amundsen Basin (Polyakov et al.
287 2013). For the winters of 2014-2015 and 2015-2016, estimates of δF_h were comparable to
288 upward heat fluxes of about 3-4 W m⁻² from 2007-2008. We attribute the decrease of δF_h in

289 2015-2016 (cf. Polyakov et al. 2017) to an anomalous freshening event in the upper ocean. This
290 freshening is evident in data collected at mooring M1₃ (**Fig. 8**) which shows that strong upper
291 (<75 m) ocean stratification (evidenced by high N^2 values) in 2016 precluded seasonal
292 ventilation beyond the SML. Stronger stratification in winter 2015 (compared with winters of
293 2014 and 2017, **Fig. 8d**) limited seasonal ventilation to the upper ~115m, thus not extending
294 deeply enough to reach the main pool of AW heat (**Fig. 8b**). In consequence the heat flux is
295 limited. The strongest heat flux is inferred for winter 2017-2018 and is associated with the
296 weakest stratification (**Fig. 5**), providing further evidence for the key role of stratification in
297 mediating upper ocean ventilation.

298 The new estimates of seasonal ventilation of heat evaluated from the δF_h for the winter
299 seasons of 2016-2017 and 2017-2018 are equivalent to 78 ± 4 and 93 ± 29 cm reductions in ice
300 growth, respectively, for the eastern EB (**Fig. 7**), given that one year of a heat flux of 1 W/m^2 in
301 isolation is equivalent to about 10 cm of sea ice loss. This represents a two-fold increase in the
302 sea ice loss rate compared to that estimated for 2013-14 (54 cm) and 2014-2015 (40 cm)
303 (Polyakov et al. 2017), and so partially explains intensified eastern EB sea ice loss in more recent
304 years (Onarheim et al. 2018; Stroeve and Notz 2018).

305 Time series from the shallower moorings (M1₂ and M1₃) show strong seasonal variations in
306 the AW core temperature, which may be associated with seasonal displacement of the AW core
307 relative to the slope (e.g., Baumann et al. 2018). However, the consistently low correlation
308 between Q and the AW core temperature records, for all mooring sites (**Fig. 9**), implies that
309 cross-slope shifts in AW temperature core are not a major driver of the seasonal variation in Q in
310 the halocline. The correlation between Q and AW core temperature at the shallowest mooring
311 (M1₂) where currents are strongest is also weak ($R = 0.29$) indicating that advection does not

312 provide a significant contribution to the seasonal variability of Q . This evidence is consistent
313 with the results of Polyakov et al. (2017) who argued that the in-phase seasonal maxima and
314 minima of wavelet transforms of Q at all mooring sites suggests that the observed winter
315 ventilation is driven by surface cooling and sea-ice formation—and not by lateral advection.
316 They reasoned that spatially varying water transports across the slope, ranging from 13 cm/s
317 (measured over the upper continental slope (250-700 m) by moorings M1₁ and M1₂) to 1-2 cm/s
318 (measured at 2700 m and deeper, at mooring locations M1₄, M1₅ and M1₆) make the in-phase
319 pattern of the seasonal signal at all moorings impossible to explain using the advective
320 mechanism. Furthermore, mooring M1₆ which was farthest from the near-slope boundary
321 current, in the ocean interior, yielded estimates for F_h which magnitudes and phases are
322 consistent with estimates from the other moorings deployed on the eastern EB continental slope
323 in 2013–2015 (Polyakov et al., 2017).

324 The one-dimensional approach adopted here can be further validated by considering the
325 magnitude of the lateral temperature gradient necessary to explain the estimated heat flux, if
326 advection were to dominate. In assuming an along slope current speed of 2 cm/s requires that the
327 lateral temperature gradient dT/dx must be five times larger than that observed Fram Strait –
328 central Laptev Sea slope temperature decrease of 1.8°C [= 3.0 – 1.2] over ~2400km so $dT/dx =$
329 0.75×10^{-3} °C/km to explain the estimated heat flux. Another potential contributor to the observed
330 ventilation rates are lateral eddy fluxes. Ventilation of halocline by eddies is, however, difficult
331 to quantify using available data. Nevertheless, considering that the typical time of eddy passing
332 across the mooring site is about a week with the average frequency about one eddy per
333 month (Pnyushkov et al., 2018b), it is unlikely that eddies can significantly contribute to changes

334 of the heat content at seasonal time scales. These considerations imply the uncertainty in the 1D
335 flux calculation from lateral advection and diffusion is small.

336 **5. Discussion and Conclusions**

337 Time series measurements from a 15-year mooring record in the eastern EB of the Arctic Ocean
338 demonstrate that the previously identified weakening of stratification over the halocline, which
339 isolates intermediate depth AW from the sea surface, over the period 2003 - 2015 (e.g.,
340 Polyakov et al. 2017, 2018), has continued at an increasing rate in more recent years (2015-
341 2018). In consequence, oceanic heat fluxes for the winters of 2016-2018 are estimated to be
342 greater than 10 Wm^{-2} . These fluxes are substantially larger than the previously reported winter
343 estimates for the region for 2007-2008 of $3\text{-}4 \text{ Wm}^{-2}$ (Lenn et al., 2009; Polyakov et al., 2019),
344 and comparable to the estimates for the winters of 2013-2015 (Polyakov et al. 2017), implying a
345 significant enhancement of the role of oceanic heat in this region in recent years.

346 Moreover, the increased vertical heat fluxes have been accompanied by increased upper-
347 ocean current speeds $|\mathbf{U}|$ and the vertical shear in the horizontal velocities $|\mathbf{U}_z|$ over the period
348 2015–2018 (Polyakov et al. 2020b). Using mooring observations from 2003 to 2018, these
349 authors showed that $|\mathbf{U}|$ and $|\mathbf{U}_z|$ in the upper 60 m of the water column increased by about 20%
350 and 40%, respectively. In the lower halocline (110-140 m), $|\mathbf{U}|$ was generally larger after 2008,
351 increasing on average from 2.5-3.5 cm/s in 2003–2008 to about 4-5 cm/s in 2009–2018 (**Fig.**
352 **5c,d**) although the change was not as strong in very recent years, 2016 and 2018 when compared
353 to 2009–2015. There is also clear transition in $|\mathbf{U}_z|$, with significantly larger shears evident post-
354 2010, and in particular in the summer of 2018 (**Fig. 5c,d**). However, Pnyushkov et al. (2018)
355 found no significant change in the mean along-slope water transport over the same period.

356 The combination of reduced stratification and increased shear implies a decreases the gradient
357 Richardson number, Ri , defined in section 3 (**Fig. 5e,f**), consistent with an increased turbulent
358 heat flux, associated with vertical mixing by shear instabilities. Although the Ri estimates are
359 based on 20m vertical resolution measurements, they show a clear trend towards reduced
360 dynamic stability which may be interpreted as a tendency towards increased turbulent mixing in
361 recent years, coincident with the increase in maximum halocline heat content (**Fig. 6**). This
362 tendency is particularly strong in 2018 with amplified velocity shear in the relatively weakly
363 stratified upper ocean (**Fig. 5**).

364 The increased shear and weakening of stratification as prerequisites for enhanced turbulent
365 mixing are consistent with the recent transition in the upper ocean to conditions previously
366 unique to the western Nansen Basin, a process called ‘atlantification’ (Polyakov et al. 2017).
367 Our analyses confirm that, in part, the loss of stratification in the eastern EB halocline can be
368 attributed to processes originating upstream. For example, the change in halocline salinity, the
369 main contributor to water column stability in the eastern EB, is correlated with upper ocean
370 salinity changes in the northern Barents Sea with a lag of approximately 2 years (**Fig. 10**) (Lind
371 et al. 2018), revealing coherent interannual variability between the two regions. In the Barents
372 Sea, these changes were found to be closely linked to declines in sea ice imports to the Barents
373 Sea (Lind et al., 2018; Barton et al., 2018). The shift towards higher salinities in the eastern EB
374 lag the changes in the northern Barents Sea by about 1 year (**Fig. 10**), implying an eastward
375 lateral progression of the ‘atlantification’. Shelf-basin interactions may also be contributing to
376 the observed warming (e.g. Timmermans et al., 2018).

377 Our observations point to the shift of this region of the eastern Arctic Ocean towards a new
378 regime that is more typical of the continental slope regions of the western Nansen Basin where

379 surface conditions are strongly influenced by oceanic heat imported from the Atlantic Ocean
380 (**Fig. 11**). The flux of AW heat to the sea ice cover and the atmosphere has increased, during the
381 winter season, from an average of 3-4 W/m² in 2007-2008 to >10 W/m² in 2016-2018,
382 equivalent to more than a two-fold reduction of winter ice growth over the last decade.

383 The process described here represents a positive feedback, analogous to the ice-albedo
384 feedback, since increased ocean heat flux to the sea surface reduces ice thickness and increases
385 its mobility, increasing atmospheric momentum flux into the ocean and reducing the damping of
386 surface-intensified baroclinic tides (Carr et al., 2019). We refer to this process as the “ice/ocean-
387 heat” feedback. As with the ice-albedo feedback, the contribution of the ice/ocean-heat feedback
388 to long-term sea ice trends depends on the seasonal variability of several factors that affect
389 mixing rates including sea ice concentration and thickness, baroclinic tidal response to
390 seasonally varying stratification, and wind stress impacts on sea ice and on AW shoaling. The
391 transition in dominant mixing regime from double diffusion to shear-driven mixing also affects
392 the relative magnitudes of buoyancy fluxes due to heat and salinity transports; the vertical
393 diffusivities for heat and salt are the same in shear-driven turbulence, but are different for double
394 diffusion (Kelley, 1984). Coincident vertical nutrient fluxes, which support oceanic primary
395 productivity, food web structure and carbon export from the atmosphere to the seabed (Bluhm et
396 al. 2015; Falk-Peterson et al. 2015), will also increase. Moreover, the nutricline has shoaled in
397 recent years (relieving nutrient limitations, **Fig. 1d**) which coupled with declining sea ice cover
398 (relieving light limitations), both influenced by atlantification, and so could lead to regional-
399 scale enhancement of biological productivity in the central Arctic Ocean.

400 As ice thins – through atmospheric forcing, changing ocean heat fluxes, and feedbacks –
401 upper-ocean stratification is responding and a new Arctic state is emerging which may not be

402 easily reversed. For example, a large anomaly in AW heat input coupled with shoaling may lead,
403 through the ice/ocean-heat feedback, to an expanding and more permanent Atlantic-dominated
404 state wherein the hydrographic structure of the halocline no longer provides sufficient insulation
405 between the intermediate depth AW and the sea ice, even when the heat flux associated with the
406 AW is relaxed. This potential for a permanent transition of the eastern Arctic to a new state,
407 emphasizes the pressing need for the incorporation of improved mixing schemes into Arctic
408 climate models in order that they better simulate the evolving halocline stratification and its
409 impact on sea ice state.

410 **Appendix A1. Building Long-Term Time Series**

411 Changes in the 110-140 m (halocline) layer at the M1₄ mooring site shown in **Fig. 5** were
412 documented using MMP records for 2003-2007 and 2013-2018, SBE37 records from M1_g
413 mooring in 2008–2010, and ADCP records for 2008-2010. This layer is the key part of the lower
414 halocline water (**Fig. 1a,b**) and has sufficient data coverage for the task. All original mooring
415 data were processed to make them comparable. We filtered MMP vertical profiles with a
416 running-mean filter to reduce resolution to 4 m, equivalent to the 2013-2018 ADCP
417 observations. We subsampled ADCP and SBE37 data in time to match coarser MMP temporal
418 resolution. The vertical shear is calculated consistently using gradients over 20 m vertical scale.
419 Reconstruction of the record at the M1₄ mooring site in 2013-2018 using MMP data from nearby
420 moorings is described below.

421 There were no MMP measurements within the 110-140m depth range at the M1₄ mooring in
422 2013-2015 and 2015-2018 (**Table 1**). Records for these years and depth range were
423 reconstructed using weighted interpolated estimates from the neighboring M1₃ and M1₅
424 moorings.

425 This approach is justified by the observed monotonic cross-slope change of current speed
 426 from M1₃, M1₄, and M1₅ mooring records for the depth ranges where overlapping data is
 427 available for the three moorings (**Fig. A1**). Estimates of buoyancy frequency N derived from
 428 temperature and salinity provided by these three moorings are statistically indistinguishable (**Fig.**
 429 **A1**).

430 Multiple regression is used to further validate the use of records from moorings M1₃ and M1₅
 431 to reconstruct time series of temperature, salinity, and current speed at mooring M1₄ for 2013-
 432 2018. The model of multiple regression is

$$433 \quad Y = \beta_0 + \beta_1 X_1 + \beta_2 X_2, \quad (1)$$

$$434 \quad \text{where } \beta_1 = \frac{r_{YX_1} - r_{YX_2} r_{X_1X_2}}{1 - r_{X_1X_2}^2} \frac{\sigma_Y}{\sigma_{X_1}}, \quad \beta_2 = \frac{r_{YX_2} - r_{YX_1} r_{X_1X_2}}{1 - r_{X_1X_2}^2} \frac{\sigma_Y}{\sigma_{X_2}}, \quad \text{and } \beta_0 = \bar{Y} - \beta_1 \bar{X}_1 + \beta_2 \bar{X}_2,$$

435 overbar denotes means, σ denotes standard deviations, r is used to denote cross-correlation
 436 coefficients, and random error term is neglected. For independent parameters X_1 and X_2 time
 437 series from M1₃ and M1₅ moorings are used, time series from M1₄ is used as the dependent
 438 variable Y . We neglected the high-frequency part of the records by applying low-pass three-
 439 month running mean filtering to each time series used in the tests because in this study we
 440 mainly focus on longer-term (interannual) trends and changes. Evidence for the validity of this
 441 approach is provided in **Fig. A2**.

442 **Acknowledgments.** The ship-based oceanographic observations in the eastern EB and Laptev
 443 Sea were conducted under the framework of the NABOS project with support from NSF (grants
 444 AON-1203473 and AON-1947162). Analyses presented in this paper are supported by NSF
 445 grants 1708427 and 1708424. The contributions from TPR and MAJ were supported by
 446 PEANUTS (NE/R01275X/1 and 03F0804A), part of the Changing Arctic Ocean programme,

447 jointly funded by the UKRI Natural Environment Research Council (NERC) and the German
448 Federal Ministry of Education and Research (BMBF). This paper is based in part on ideas
449 discussed at an international workshop on pan-Arctic marine systems in Motovun Croatia,
450 organized by P. Wassmann and supported by funding from Arctic SIZE
451 (<http://site.uit.no/arcticsize/>). All mooring data used in this study are available at
452 <https://arcticdata.io/catalog/#view/arctic-data> (doi: 10.18739/A2N37R and
453 10.18739/A2HT2GB80).

454

455

456

457 **References**

- 458 Barton, B. I., Y.-D. Lenn, and C. Lique, 2018: Observed atlantification of the Barents Sea causes
459 the polar front to limit the expansion of winter sea ice. *J. Phys. Oceanogr.*, **48**(8), 1849-
460 1866.
- 461 Baumann, T. M., I. V. Polyakov, A. V. Pnyushkov, R. Rember, V. V. Ivanov, M. B. Alkire, I.
462 Goszczko, and E. C. Carmack, 2018: On the seasonal cycles observed at the continental slope
463 of the Eastern Eurasian Basin of the Arctic Ocean. *J. Phys. Oceanogr.*, **48**, 1451-1470, DOI:
464 10.1175/JPO-D-17-0163.1.
- 465 Bluhm B. A., K. N. Kosobokoba, and E. C. Carmack, 2015: A tale of two basins: An integrated
466 physics and biology perspective of the deep Arctic Ocean. *Progress in Oceanography*
467 <http://dx.doi.org/10.1016/j.pocean.2015.07.011>.
- 468 Carmack E., I. Polyakov, L. Padman, I. Fer, E. Hunke, J. Hutchings, J. Jackson, D. Kelley, R.
469 Kwok, C. Layton, D. Perovich, O. Persson, B. Ruddick, M.-L. Timmermans, J. Toole, T.
470 Ross, S. Vavrus, and P. Winsor, 2015: The new Arctic: Towards quantifying the increasing
471 role of oceanic heat in sea ice loss, *BAMS*, **96**(12), 2079-2105, 10.1175/BAMS-D-13-
472 00177.1.
- 473 Carr, M., P. Sutherland, A. Haase, K.- U. Evers, I. Fer, A. Jensen, H. Kalisch, J. Berntsen,
474 E. Părău, Ø. Thiem and PA. Davies (2019). Laboratory Experiments on Internal Solitary
475 Waves in Ice- Covered Waters. *Geophysical Research Letters*, 2019GL084710
- 476 Cavalieri, D. J., C. L. Parkinson, P. Gloersen, and H. J. Zwally. 1996, updated yearly. *Sea Ice*
477 *Concentrations from Nimbus-7 SMMR and DMSP SSM/I-SSMIS Passive Microwave Data,*
478 *Version 1*. Boulder, Colorado USA. NASA National Snow and Ice Data Center Distributed
479 Active Archive Center. doi: <https://doi.org/10.5067/8GQ8LZQVL0VL>.
- 480 Falk-Petersen, S., V. Pavlov, J. Berge, F. Cottier, K. M. Kovacs, and C. Lydersen, 2015: At the
481 rainbow's end: High productivity fueled by winter upwelling along an Arctic shelf. *Polar Biol.*,
482 **38**, 5–11.
- 483 Fer, I., 2009: Weak vertical diffusion allows maintenance of cold halocline in the central Arctic.
484 *Atmos. Ocean. Sci. Lett.*, **2**, 148-152.

485 Fer, I., R. Skogseth, and F. Geyer, 2010: Internal waves and mixing in the Marginal Ice Zone
486 near the Yermak Plateau. *J. Phys. Oceanogr.* **40**(7), 1613-1630. doi:
487 10.1175/2010JPO4371.1.

488 Frances, J. A., S. J. Vavrus, and J. Cohen, 2017: Amplified arctic warming and mid-latitude
489 weather: new perspectives on emerging connections. *Wiley Interdisciplinary Reviews:*
490 *Climate Change*, **8**(5), e474.

491 Garcia- Serrano, J., C. Frankignoul, G. Gastineau, and A. de la Camera, 2015: On the
492 predictability of the winter euro-atlantic climate: lagged influence of autumn arctic sea
493 ice. *J. Clim.*, **28**(13), 5195-5216.

494 Graham, R. M., *et al.*, 2019: Winter storms accelerate the demise of sea ice in the Atlantic sector
495 of the Arctic Ocean, *Scientific Reports*, **9**, 9222, 10.1038/s41598-019-45574-5.

496 Kelley, D., 1984. Effective diffusivities within oceanic thermohaline staircases. *J. Geophys.*
497 *Res.: Oceans*, **89**(C6), 10484-10488.

498 Kolstad, E., and J. Screen, 2019: Non-stationary relationship between autumn arctic sea ice and
499 the winter north atlantic oscillation, *Geophys. Res. Lett.*, **46**(13), 7583-7591.

500 Kwok, R., 2018: Arctic sea ice thickness, volume, and multiyear ice coverage: losses and
501 coupled variability (1958–2018), *Environ. Res. Lett.* **13**, 105005.

502 Lenn, Y.-D., P. Wiles, S. Torres-Valdes, E. Abrahamsen, T. Rippeth, J. H. Simpson, S. Bacon, S.
503 Laxon, I. Polyakov, V. Ivanov, and S. Kirillov, 2009: Vertical mixing at intermediate
504 depths in the Arctic boundary current, *Geophys. Res. Lett.*, **36**, L05601, doi:
505 10.1029/2008GL036792.

506 Lind, S., R. B. Ingvaldsen, and T. Furevik, 2018: Declining sea ice import and freshwater loss
507 causes Arctic warming hotspot. *Nature Climate Change*, **8**(7), doi:10.1038/s41558-018-
508 0205-y.

509 Manabe, S., and R. J. Stouffer, 1980: Sensitivity of a global climate model to an increase of CO₂
510 concentration in the atmosphere. *J. Geophys. Res.*, **85**, 5529-5554.

- 511 Onarheim, I. H., T. Eldevik, L. H. Smedsrud, and J. C. Stroeve, 2018: Seasonal and regional
512 manifestation of Arctic sea ice loss. *J. Climate*, **31**, 4917-4932, DOI: 10.1175/JCLI-D-17-
513 0427.1.
- 514 Perovich, D. K., J. A. Richter-Menge, K. F. Jones, and B. Light, 2008: Sunlight, water, and ice:
515 Extreme Arctic sea ice melt during the summer of 2007, *Geophys. Res. Lett.*, **35**, L11501,
516 doi:10.1029/2008GL034007.
- 517 Polyakov, I. V., A. Beszczynska, E. C. Carmack, I. A. Dmitrenko, E. Fahrbach, I. E. Frolov, R.
518 Gerdes, E. Hansen, J. Holfort, V. V. Ivanov, M. A. Johnson, M. Karcher, F. Kauker, J.
519 Morison, K. A. Orvik, U. Schauer, H. L. Simmons, Ø. Skagseth, V. T. Sokolov, M. Steele,
520 L. A. Timokhov, D. Walsh, and J. E. Walsh, 2005: One more step toward a warmer Arctic.
521 *Geophys. Res. Lett.*, **32**, L17605, doi:10.1029/2005GL023740.
- 522 Polyakov, I. V., L. A. Timokhov, V. A. Alexeev, S. Bacon, I. A. Dmitrenko, L. Fortier, I. E. Frolov,
523 J.-C. Gascard, E. Hansen, V. V. Ivanov, S. Laxon, C. Mauritzen, D. Perovich, K. Shimada,
524 H. L. Simmons, V. T. Sokolov, M. Steele, and J. Toole, 2010: Arctic Ocean warming reduces
525 polar ice cap, *J. Phys. Oceanogr.*, DOI: 10.1175/2010JPO4339.1, **40**, 2743–2756.
- 526 Polyakov, I. V., A. V. Pnyushkov, R. Rember, L. Padman, E. C. Carmack, and J. Jackson, 2013:
527 Winter convection transports Atlantic Water heat to the surface layer in the eastern Arctic
528 Ocean, *J. Phys. Oceanogr.*, **43**(10), 2148–2162, DOI: 10.1175/JPO-D-12-0169.1.
- 529 Polyakov, I. V., A. V. Pnyushkov, M. Alkire, I. M. Ashik, T. Baumann, E. Carmack, I.
530 Goszczko, V. Ivanov, T. Kanzow, R. Krishfield, R. Kwok, A. Sundfjord, J. Morison, R.
531 Rember, and A. Yulin, 2017: Greater role for Atlantic inflows on sea-ice loss in the
532 Eurasian Basin of the Arctic Ocean, *Science*, **356**(6335), 285-291, doi:
533 10.1126/science.aai8204.
- 534 Polyakov, I. V., A. V. Pnyushkov, and E. C. Carmack, 2018: Stability of the arctic halocline: A
535 new indicator of arctic climate change. *Environ. Res. Letts.*, **13**, 125008,
536 <https://doi.org/10.1088/1748-9326/aaec1e>.
- 537 Polyakov, I. V., L. Padman, Y.-D. Lenn, A. V. Pnyushkov, R. Rember and V. V. Ivanov, 2019:
538 Eastern Arctic Ocean diapycnal heat fluxes through large double-diffusive steps, *J. Phys.*
539 *Oceanogr.*, **49**, 227-246, DOI: 10.1175/JPO-D-18-0080.1.

540 Polyakov, I. V., M. B. Alkire, B. A. Bluhm, K. Brown, E. C. Carmack, M. Chierici, S. Danielson,
541 I. Ellingsen, E. A. Ershova, K. Gårdfeldt, R. B. Ingvaldsen, A. V. Pnyushkov, D. Slagstad,
542 P. Wassmann, 2020a: Borealization of the Arctic Ocean in response to anomalous
543 advection from sub-arctic seas, *Frontiers in Marine Science*. Submitted.

544 Polyakov, I. V., T. P. Rippeth, I. Fer, T. M. Baumann, E. C. Carmack, V. V. Ivanov, M. Janout,
545 L. Padman, A. V. Pnyushkov, and R. Rember, 2020b: Transition to a new ocean dynamic
546 regime in the eastern Arctic Ocean. *Geophys. Res. Lett.* Submitted.

547 Pnyushkov, A., Polyakov, I., Ivanov, V., Aksenov, Ye., Coward, A., Janout, M., and Rabe, B.
548 2015: Structure and variability of the boundary current in the Eurasian Basin of the Arctic
549 Ocean. *Deep-Sea Res.-I*, **101**(7), p.80-97, doi:10.1016/j.dsr.2015.03.001.

550 Pnyushkov, A. V., I. V. Polyakov, R. Rember, V. V. Ivanov, M. B. Alkire, I. M. Ashik, T. M.
551 Baumann, G. V. Alekseev, and A. Sundfjord, 2018: Heat, salt, and volume transports in the
552 eastern Eurasian Basin of the Arctic Ocean from 2 years of mooring observations. *Ocean
553 Sci.*, **14**, 1349-1371, <https://doi.org/10.5194/os-14-1349-2018>.

554 Pnyushkov, A., Polyakov, I. V., Padman, L., and Nguyen, A. T. 2018b: Structure and dynamics
555 of mesoscale eddies over the Laptev Sea continental slope in the Arctic Ocean, *Ocean Sci.*,
556 **14**, 1329-1347, <https://doi.org/10.5194/os-14-1329-2018>.

557 Provost, C., Sennechael, N., Miguet, J., Itkin, P., Rosel, A., Koenig, Z., Villaciers-Robineau,
558 N., and M. A. Granskog, 2017: Observations of flooding and snow-ice formation in a
559 thinner Arctic sea-ice regime during the N-ICE2015 campaign: Influence of basal ice melt
560 and storms, *J. Geophys. Res. Oceans*, **122**, 7115–7134, doi:10.1002/2016JC012011.

561 Renner, A. H. H., Sundfjord, A., Janout, M. A., Ingvaldsen, R., Beszczynska-Möller, A., Pickart,
562 R., and Pérez-Hernández, M., (2018). Variability and redistribution of heat in the Atlantic
563 Water boundary current north of Svalbard. *J. Geophys. Res.: Oceans*, **123**, 6373–6391.
564 <https://doi.org/10.1029/2018JC013814>

565 Rippeth, T. P., Lincoln, B. J., Lenn, Y.-D., Green, J. M., Sundfjord, A., and Bacon, S. 2015: Tide-
566 mediated warming of Arctic halocline by Atlantic heat fluxes over rough topography. *Nature
567 Geosci.* **8**, 191–194, doi:10.1038/ngeo2350.

568 Shibley, N. C., M.-L. Timmermans, J. R. Carpenter, and J. M. Toole, 2017: Spatial variability of
569 the Arctic Ocean's double-diffusive staircase, *J. Geophys. Res. Oceans*, **122**, 980-994,
570 doi:10.1002/2016JC012419.

571 Silvester, J. M., Y.D. Lenn, J.A. Polton, T.P. Rippeth & M.M. Maqueda, M. M. (2014).
572 Observations of a diapycnal shortcut to adiabatic upwelling of Antarctic Circumpolar Deep
573 Water. *Geophys. Res. Lett.*, **41**, 7950-7956.

574 Steele, M., and T. Boyd, 1998: Retreat of the cold halocline layer in the Arctic Ocean. *J.*
575 *Geophys. Res. - Oceans.*, **103**(C5), 10419-10435.

576 Stroeve, J., and D. Notz, 2018: Changing state of Arctic sea ice across all seasons. *Env. Res.*
577 *Lett.*, **13**, 103001.

578 Timmermans, M.-L., J. Toole, and R. Krishfield, 2018: Warming of the interior Arctic Ocean
579 linked to sea ice losses at the basin margins. *Science Advances*, **4**: eaat6773.

580 Toole, J. M., M. L. Timmermans, D. K. Perovich, R. A. Krishfield, A. Proshutinsky, and J. A.
581 Richter-Menge, 2010: Influences of the ocean surface mixed layer and thermohaline
582 stratification on Arctic Sea ice in the central Canada Basin. *J. Geophys. Res.*, **115**, C10018,
583 doi:10.1029/2009jc005660.

584 Torrence, C. and G. P. Compo, 1998: A practical guide to wavelet analysis. *Bull. Amer. Meteor.*
585 *Soc.* **79**(1), 61-78.

586

Figure legends

588 **Figure 1:** Vertical profiles of (a) potential temperature θ , (b) salinity S , (c) the logarithm of squared
 589 Brunt-Väisälä frequency (N^2 , s^{-2} , a measure of water column stability; 5-point smoothing is applied)
 590 and (d) nutrients at M1₄ mooring site made on August 27, 2013, September 20, 2015, and
 591 September 2, 2018. Circulation of the intermediate Atlantic Water (AW) in the Arctic Ocean is
 592 shown schematically in (e) by red arrows. In (a), the upper part of halocline is cold halocline layer
 593 (CHL) in which salinity increases with depth while temperature remains near the freezing point.
 594 The blue box indicates the area of the Arctic Ocean with mooring positions shown in **Fig. 2**. The
 595 Canada Basin (CB), Chukchi Sea (CS), East Siberian Sea (ESS), and Barents Sea (BS) are
 596 indicated.

597 **Figure 2:** Map showing the focus of the study together with the positions of moorings and location
 598 of CTD (Conductivity-Temperature-Depth) profiles made in summer 2013, 2015, and 2018
 599 reported in this study. The Gakkel Ridge (GR) divides the Eurasian Basin (EB) into the Nansen
 600 Basin and the Amundsen Basin. The Lomonosov Ridge (LR), Novosibirskiye Islands (NI),
 601 Severnaya Zemlya (SZ), Franz Joseph Land (FJL), and Makarov Basin (MB) are indicated. Grey
 602 solid lines show depth in meters. The eastern EB region used for calculation of blue time series in
 603 **Fig. 10** is identified by green line.

604 **Figure 3:** Composite 2002–2018 time series of (a) monthly mean potential water temperature (θ)
 605 and (c) daily depth of the lower halocline boundary (H_{base}) defined by 0°C isotherm at M1₄ mooring
 606 location (for location, see **Fig. 2**). (b) Comparison of de-seasoned monthly mean time series of
 607 normalized θ anomalies from 250m of M14 mooring of the eastern EB (EEB) and lagged by 678
 608 days (as obtained from correlation analysis) F2-F3 moorings of Fram Strait; time series are
 609 normalized by their standard deviations.

610 **Figure 4:** Depth–time diagram of potential temperature θ (°C) from M1₃ mooring. Black lines
 611 show the depth of the halocline base and lower Atlantic Water boundary both defined by 0°C
 612 isotherms.

613 **Figure 5:** Estimates of (left) annual and (right) summer mean (a,b) squared buoyancy frequency
 614 N^2 ($10^5 s^{-2}$), (c,d) current magnitude $|U|$ and squared vertical shear of horizontal currents $|U_z|^2$,
 615 and (e,f) proxy of Richardson number Ri for the 110–140 m depth range for the M1₄ mooring
 616 location. Statistical significance of means is shown at the 95% confidence level.

617 **Figure 6:** (Left and middle) 65-140m layer depth versus time of water temperature and annual
 618 component of heat content Q . Annual components are obtained via band-pass filtering using
 619 wavelet transformations. Horizontal black segments identify the depth of seasonal ventilation;
 620 dates identified by their ends are used to compute vertically integrated Q shown in the lower parts
 621 of panels in the right column. (Right) Vertically integrated Q for the beginning (warm phase) and
 622 end (cold phase) of seasonal ventilation (lower parts of the panels) and divergent heat fluxes δF_h
 623 (upper parts) for four moorings.

624 **Figure 7:** Time-averaged over M3, M1₂, M1₃, and M1₄ mooring records (top) vertically
 625 integrated Q for the beginning (warm phase, red bars, Q_{\max}) and end (cold phase, blue bars, Q_{\min})
 626 of seasonal ventilation of eastern EB halocline (110-140m), (middle) divergent heat fluxes δF_h
 627 (blue bars for averages with ± 1 standard error shown as black segments), and (bottom) equivalent
 628 sea ice thickness losses.

629 **Figure 8:** (a) Potential temperature, (b) annual component of heat content Q obtained by band-
 630 pass filtering of daily heat content using wavelet spectra; horizontal black segments identify the
 631 depth of seasonal ventilation, (c) salinity, and (d) squared buoyancy frequency for M1₃ mooring.

632 **Figure 9:** (left) Depth versus time diagram of potential water temperature θ ($^{\circ}\text{C}$) and (right) time
 633 series of monthly heat content Q for the 65-140m layer (blue) and AW core temperature (red) for
 634 four moorings. Low correlations between these time series $R_{Q-\theta}$ suggest that changes of Q are not
 635 related to seasonal shift of AW core relative to the slope.

636 **Figure 10:** Normalized (reduced to anomalies and divided by one standard deviation SD) annual
 637 time series of (blue) halocline salinity S in the eastern EB (EEB, from Polyakov et al. 2018) and
 638 (red) lagged by one year (as obtained from correlation analysis) upper ocean S from the northern
 639 Barents Sea (from Lind et al. 2018). Dash-dotted lines are used to fill gaps (interpolated values
 640 are *not* used for statistical estimates). Means and SDs are indicated. Trends are shown by dashed
 641 lines; all trends are statistically significant at the 95% confidence according to the Student t test.
 642 The break-point in 1999 separates periods with opposite trends.

643 **Figure 11:** Conceptual model of shift of the mixing regime in the eastern EB in recent years and
 644 associated suite of processes and state conditions including: 1) thinner, more mobile ice, 2)
 645 warmer surface mixed layer (SML), 3) weakening / retreat of cold halocline (HC) layer, 4)
 646 increased AW vertical heat flux (red arrows) and horizontal currents and their vertical shear

647 (blue arrows), 5) shoaling of upper AW boundary, and 6) replacement of DD by shear
648 instabilities as the fundamental mechanism of vertical flux.

649 **Figure A1:** 2013/15 mean estimates of (top) squared Brunt-Väisälä frequency N^2 , and current
650 speed $|U|$ for (middle) 20-60 m and (bottom) 190-230 m depth ranges where the mooring records
651 from M1₃, M1₄, and M1₅ overlap. Statistical significance of estimates for means is shown at the
652 95% confidence level.

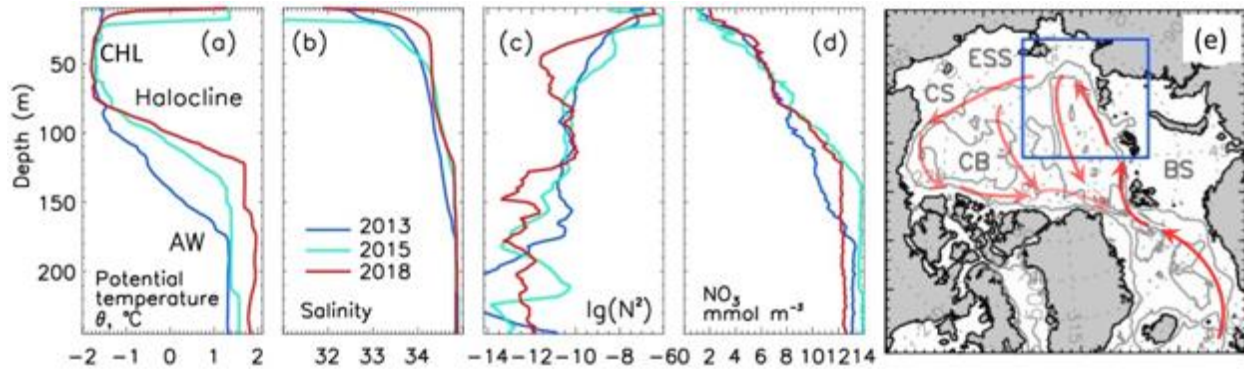
653 **Figure A2:** Multiple regression reconstruction of (a,b) salinity and (c,d) current speed $|U|$ at M1₄
654 mooring site using data from M1₃ and M1₅ moorings for 170-210m depth range. (a,c) Daily
655 (dotted) and three-month running mean smoothed time series of (a) salinity and (c) $|U|$ from M1₃,
656 M1₄, and M1₅ moorings. (b,d) Original (blue) and reconstructed (red) time series of (b) salinity
657 and (d) $|U|$ from M1₄ mooring. Relatively high correlations between the original and
658 reconstructed time series attests of good quality of reconstruction.

659
660
661
662
663
664
665
666
667
668
669
670
671
672

673

Figures

674

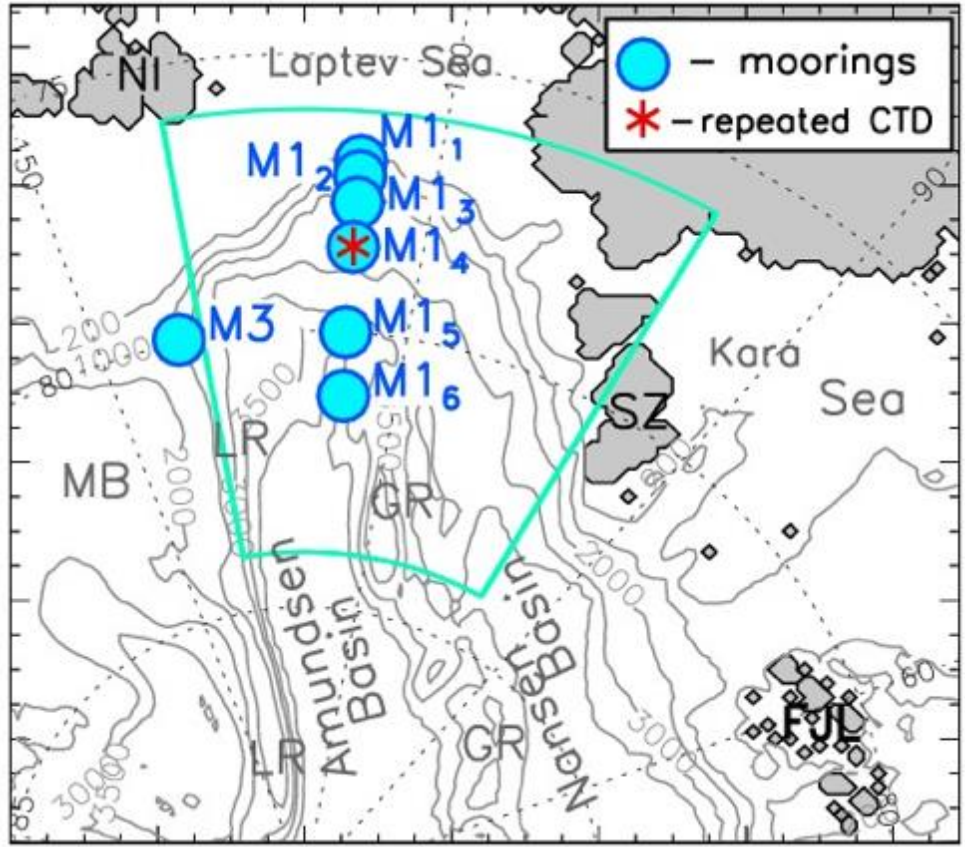


675

676 **Figure 1:** Vertical profiles of (a) potential temperature θ , (b) salinity S , (c) the logarithm of squared
677 Brunt-Väisälä frequency (N^2 , s^{-2} , a measure of water column stability; 5-point smoothing is applied)
678 and (d) nutrients at M14 mooring site made on August 27, 2013, September 20, 2015, and
679 September 2, 2018. Circulation of the intermediate Atlantic Water (AW) in the Arctic Ocean is
680 shown schematically in (e) by red arrows. In (a), the upper part of halocline is cold halocline layer
681 (CHL) in which salinity increases with depth while temperature remains near the freezing point.
682 The blue box indicates the area of the Arctic Ocean with mooring positions shown in **Fig. 2**. The
683 Canada Basin (CB), Chukchi Sea (CS), East Siberian Sea (ESS), and Barents Sea (BS) are
684 indicated.

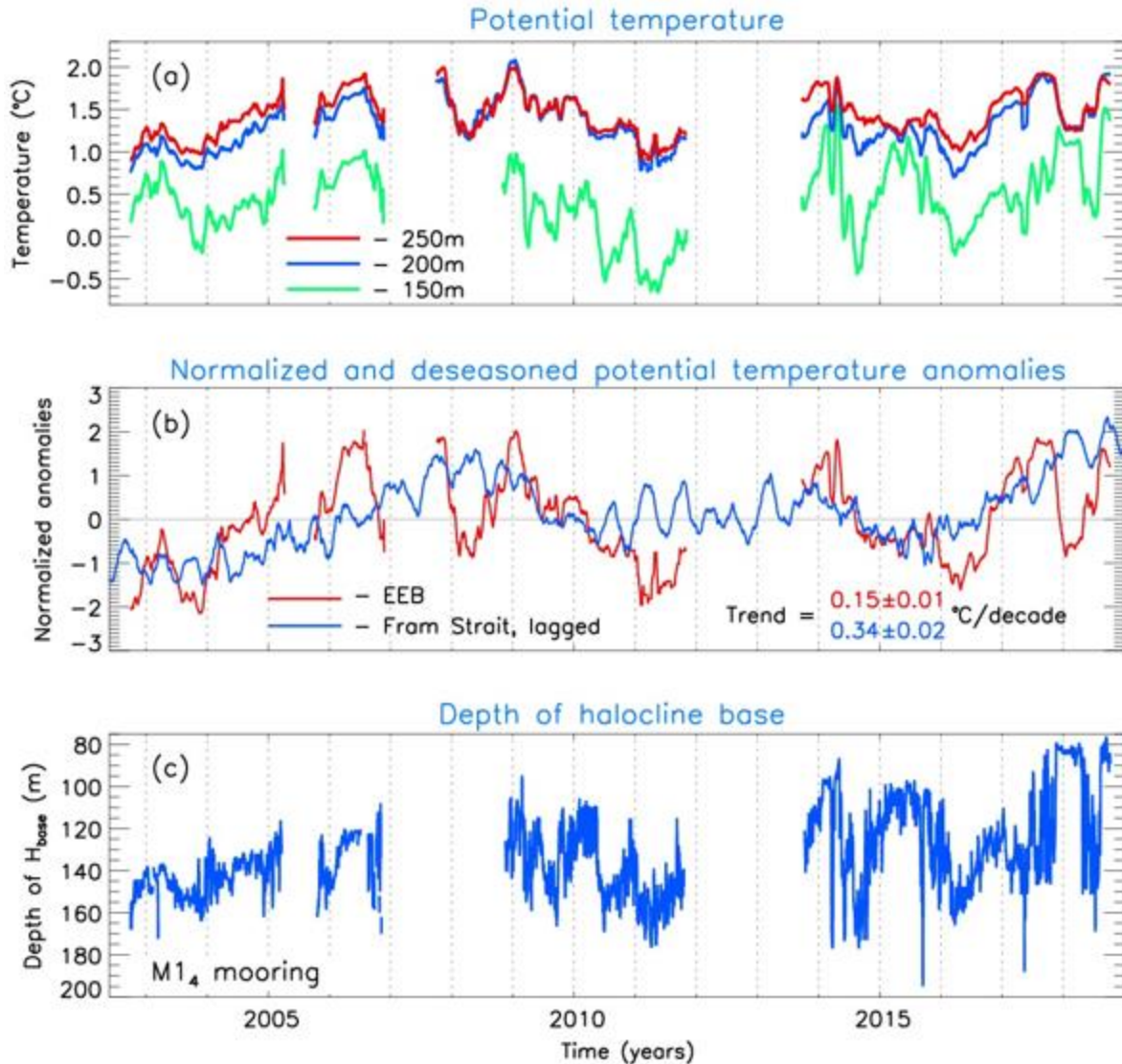
685

686

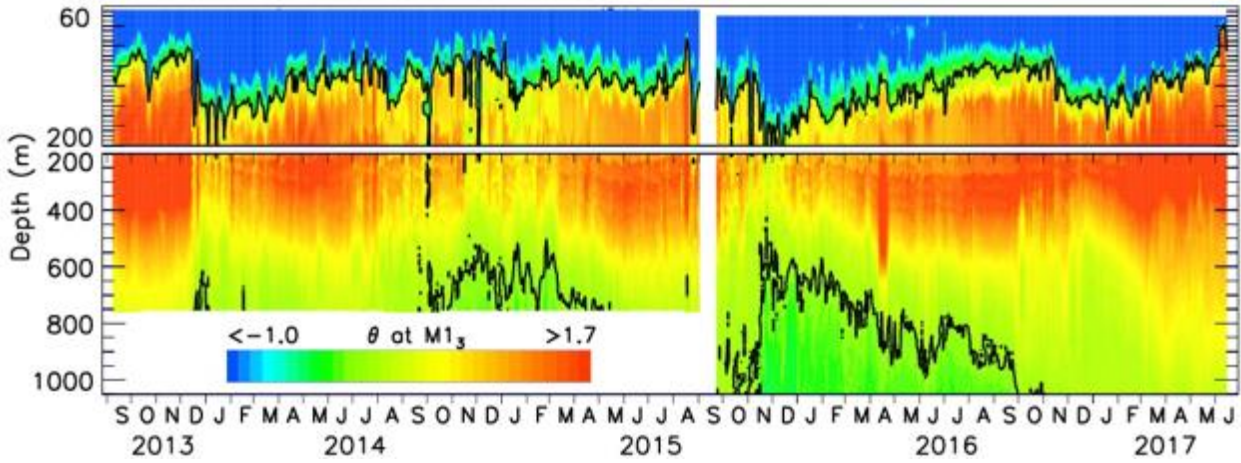


687
 688 **Figure 2:** Map showing the focus of the study together with the positions of moorings and location
 689 of CTD (Conductivity-Temperature-Depth) profiles made in summer 2013, 2015, and 2018
 690 reported in this study. The Gakkel Ridge (GR) divides the Eurasian Basin (EB) into the Nansen
 691 Basin and the Amundsen Basin. The Lomonosov Ridge (LR), Novosibirskiye Islands (NI),
 692 Severnaya Zemlya (SZ), Franz Joseph Land (FJL), and Makarov Basin (MB) are indicated. Grey
 693 solid lines show depth in meters. The eastern EB region used for calculation of blue time series in
 694 **Fig. 10** is identified by green line.

695
 696



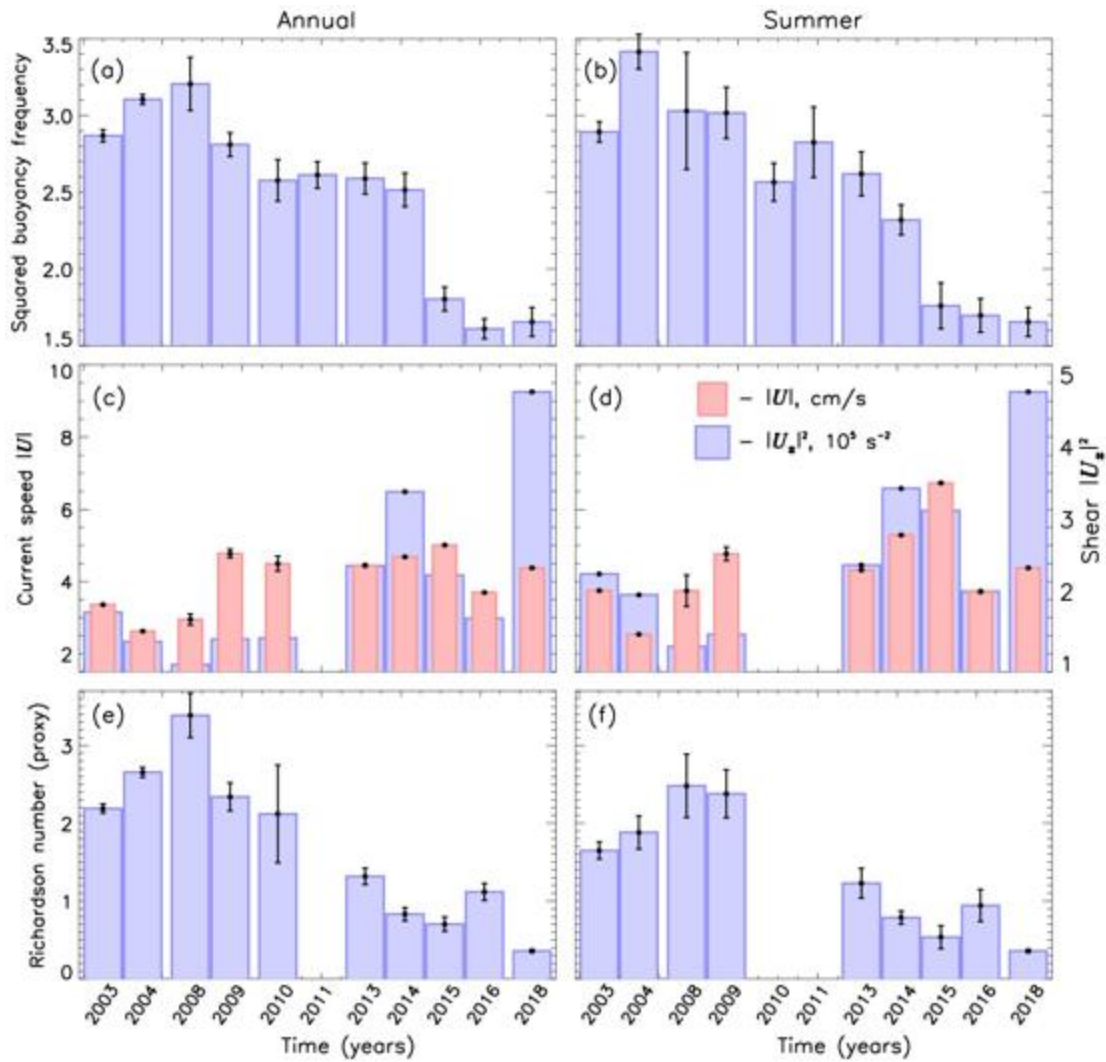
697
 698 **Figure 3:** Composite 2002 –2018 time series of (a) monthly mean potential water temperature (θ)
 699 and (c) daily depth of the lower halocline boundary (H_{base}) defined by 0°C isotherm at M1₄ mooring
 700 location (for location, see **Fig. 2**). (b) Comparison of de-seasoned monthly mean time series of
 701 normalized θ anomalies from 250m of M1₄ mooring of the eastern EB (EEB) and lagged by 678
 702 days (as obtained from correlation analysis) F2-F3 moorings of Fram Strait; time series are
 703 normalized by their standard deviations.



704

705 **Figure 4:** Depth–time diagram of potential temperature θ (°C) from M1₃ mooring. Black lines
 706 show the depth of the halocline base and lower Atlantic Water boundary both defined by 0°C
 707 isotherms.

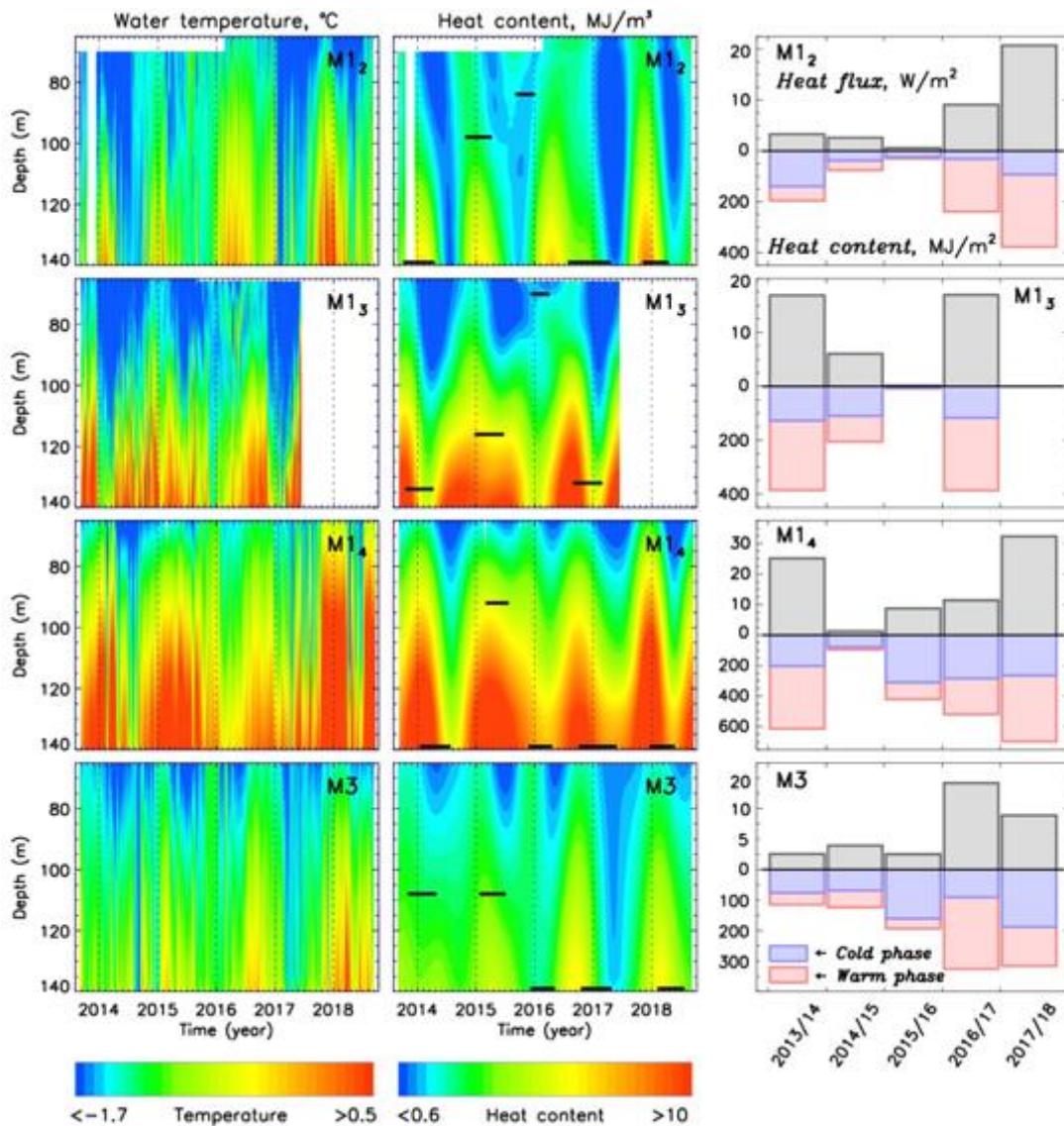
708



709

710 **Figure 5:** Estimates of (left) annual and (right) summer mean (a,b) squared buoyancy frequency
 711 N^2 (10^5 s^{-2}), (c,d) current magnitude $|U|$ and squared vertical shear of horizontal currents $|U_z|^2$,
 712 and (e,f) proxy of Richardson number Ri for the 110-140 m depth range for the M14 mooring
 713 location. Statistical significance of means is shown at the 95% confidence level.

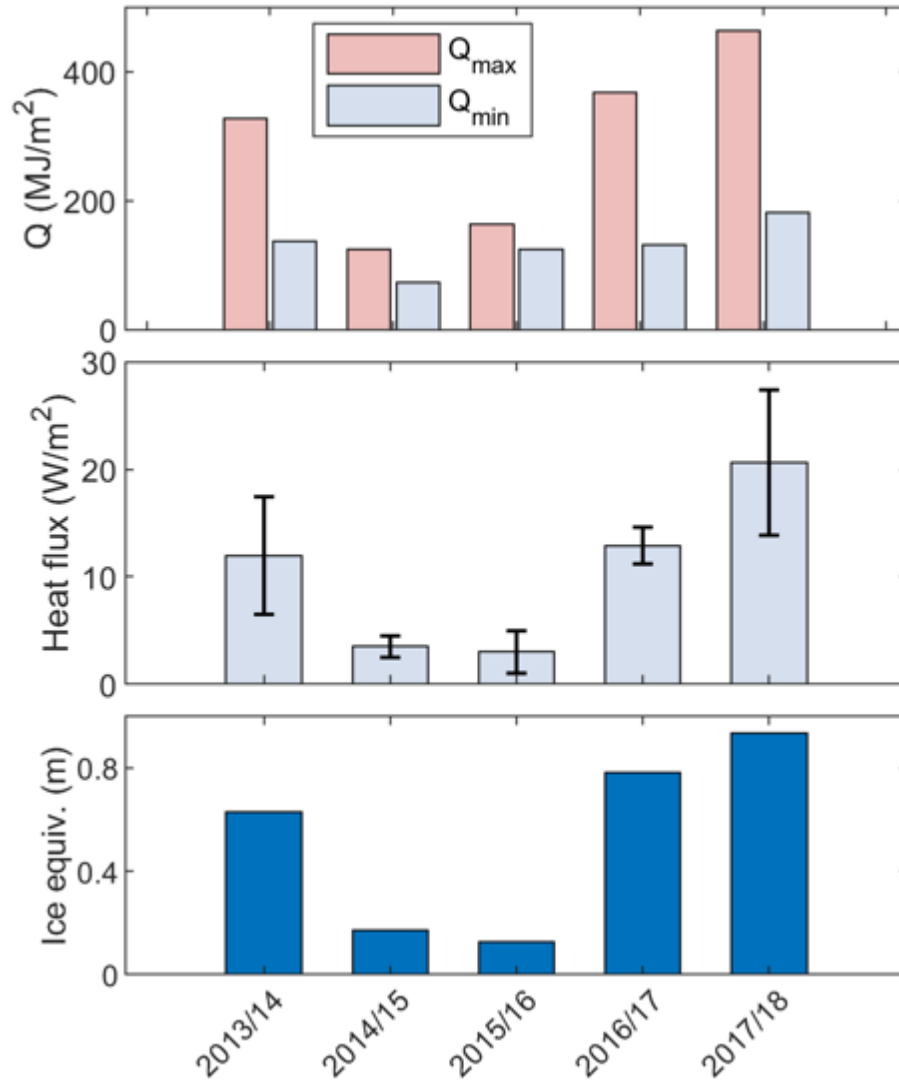
714



716

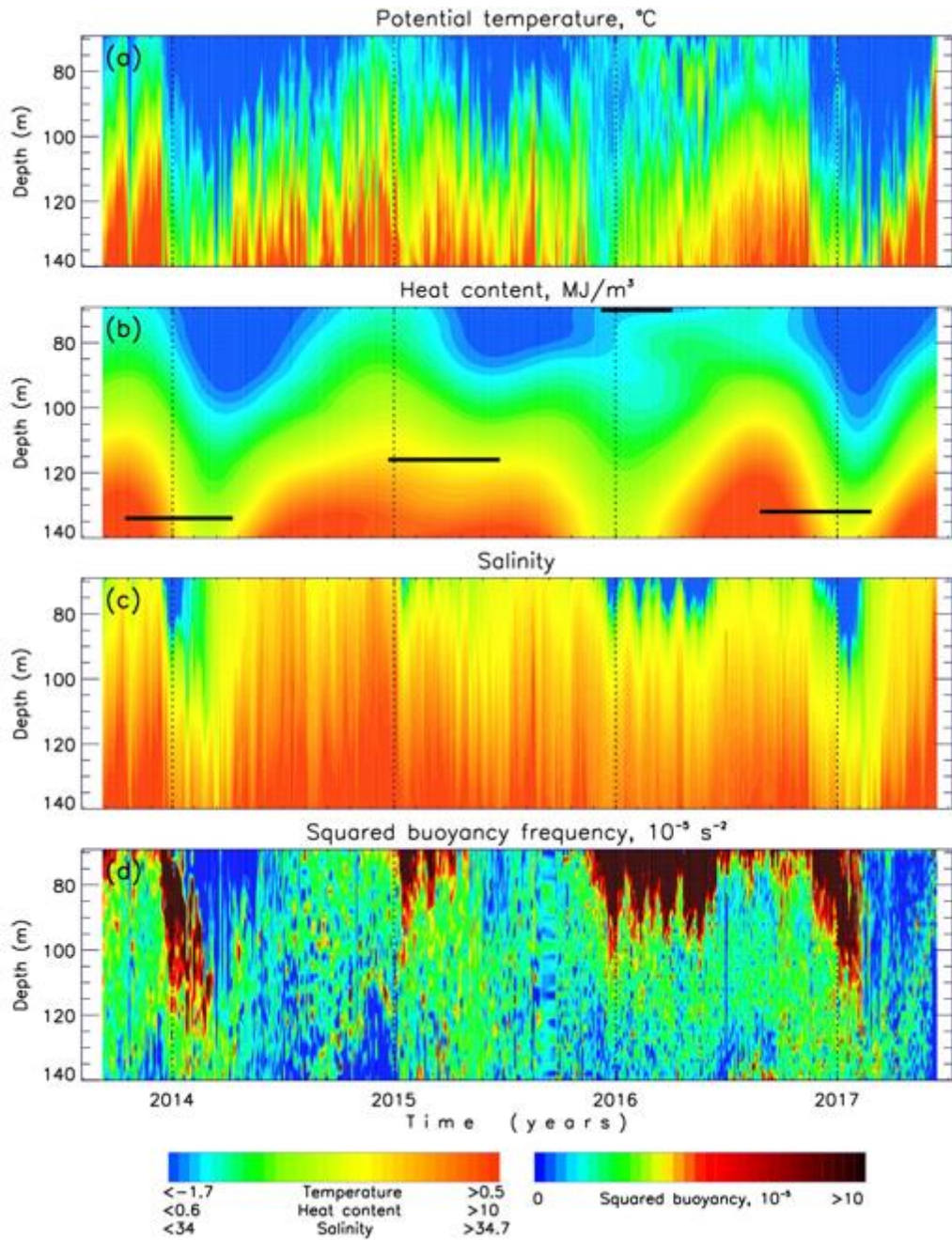
717 **Figure 6:** (Left and middle) 65-140m layer depth versus time of water temperature and annual
 718 component of heat content Q . Annual components are obtained via band-pass filtering using
 719 wavelet transformations. Horizontal black segments identify the depth of seasonal ventilation;
 720 dates identified by their ends are used to compute vertically integrated Q shown in the lower parts
 721 of panels in the right column. (Right) Vertically integrated Q for the beginning (warm phase) and
 722 end (cold phase) of seasonal ventilation (lower parts of the panels) and divergent heat fluxes δF_h
 723 (upper parts) for four moorings.

724



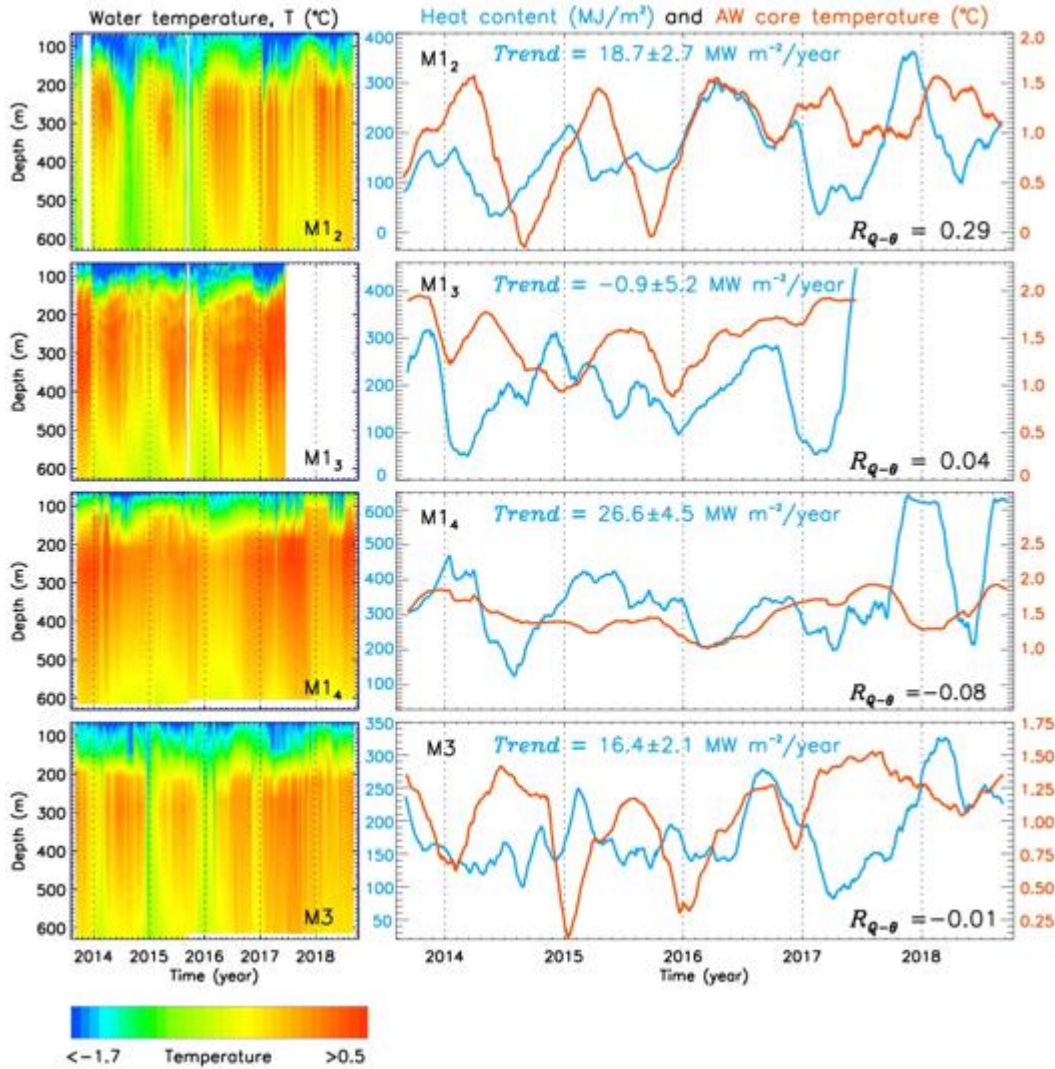
725
726

727 **Figure 7:** Time-averaged over M3, M1₂, M1₃, and M1₄ mooring records (top) vertically
 728 integrated Q for the beginning (warm phase, red bars, Q_{max}) and end (cold phase, blue bars, Q_{min})
 729 of seasonal ventilation of eastern EB halocline (110-140m), (middle) divergent heat fluxes δF_h
 730 (blue bars for averages with ± 1 standard error shown as black segments), and (bottom) equivalent
 731 sea ice thickness losses.



732

733 **Figure 8:** (a) Potential temperature, (b) annual component of heat content Q obtained by band-
 734 pass filtering of daily heat content using wavelet spectra; horizontal black segments identify the
 735 depth of seasonal ventilation, (c) salinity, and (d) squared buoyancy frequency for M1₃ mooring.



736

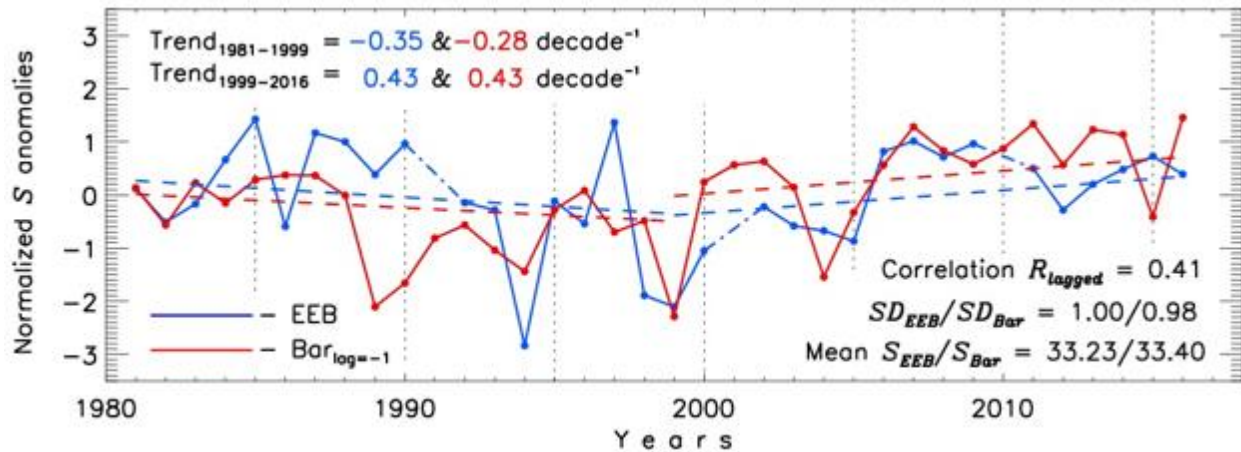
737 **Figure 9:** (left) Depth versus time diagram of potential water temperature θ (°C) and (right) time
 738 series of monthly heat content Q for the 65-140m layer (blue) and AW core temperature (red) for
 739 four moorings. Low correlations between these time series $R_{Q-\theta}$ suggest that changes of Q are not
 740 related to seasonal shift of AW core relative to the slope.

741

742

743

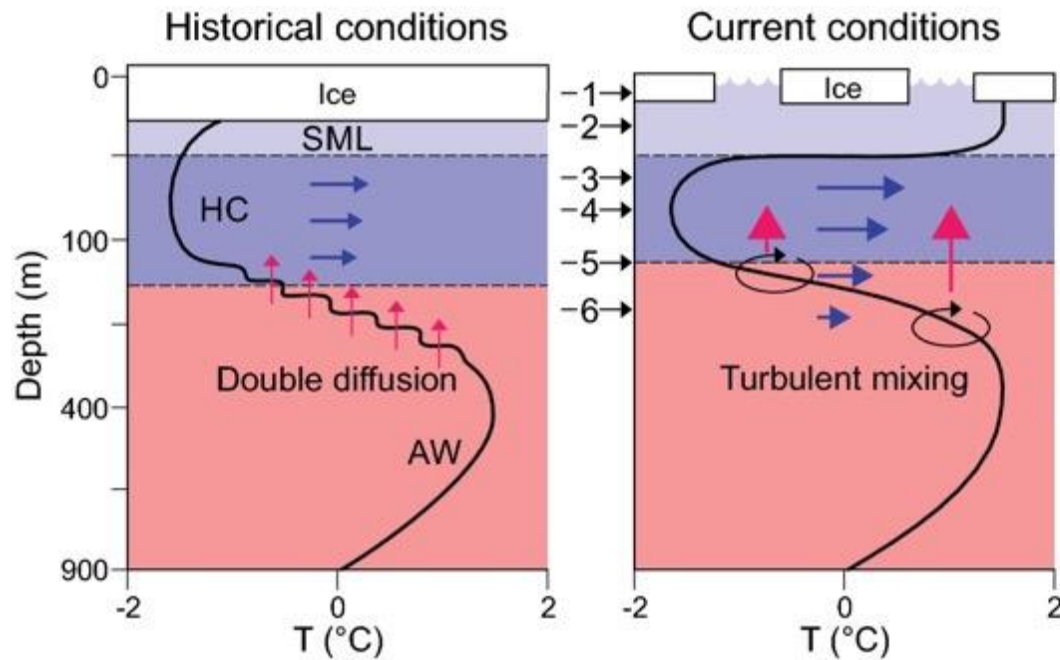
744



745

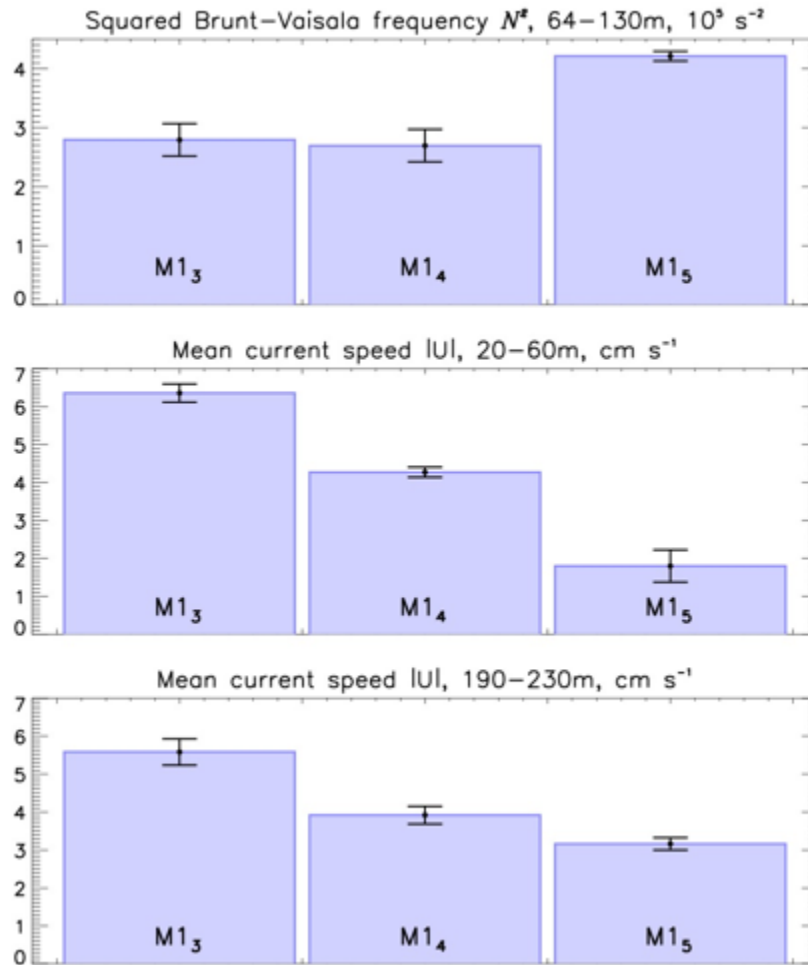
746 **Figure 10:** Normalized (reduced to anomalies and divided by one standard deviation SD) annual
 747 time series of (blue) halocline salinity S in the eastern EB (EEB, from Polyakov et al. 2018) and
 748 (red) lagged by one year (as obtained from correlation analysis) upper ocean S from the northern
 749 Barents Sea (from Lind et al. 2018). Dash-dotted lines are used to fill gaps (interpolated values
 750 are *not* used for statistical estimates). Means and SDs are indicated. Trends are shown by dashed
 751 lines; all trends are statistically significant at the 95% confidence according to the Student t test.
 752 The break-point in 1999 separates periods with opposite trends.

753



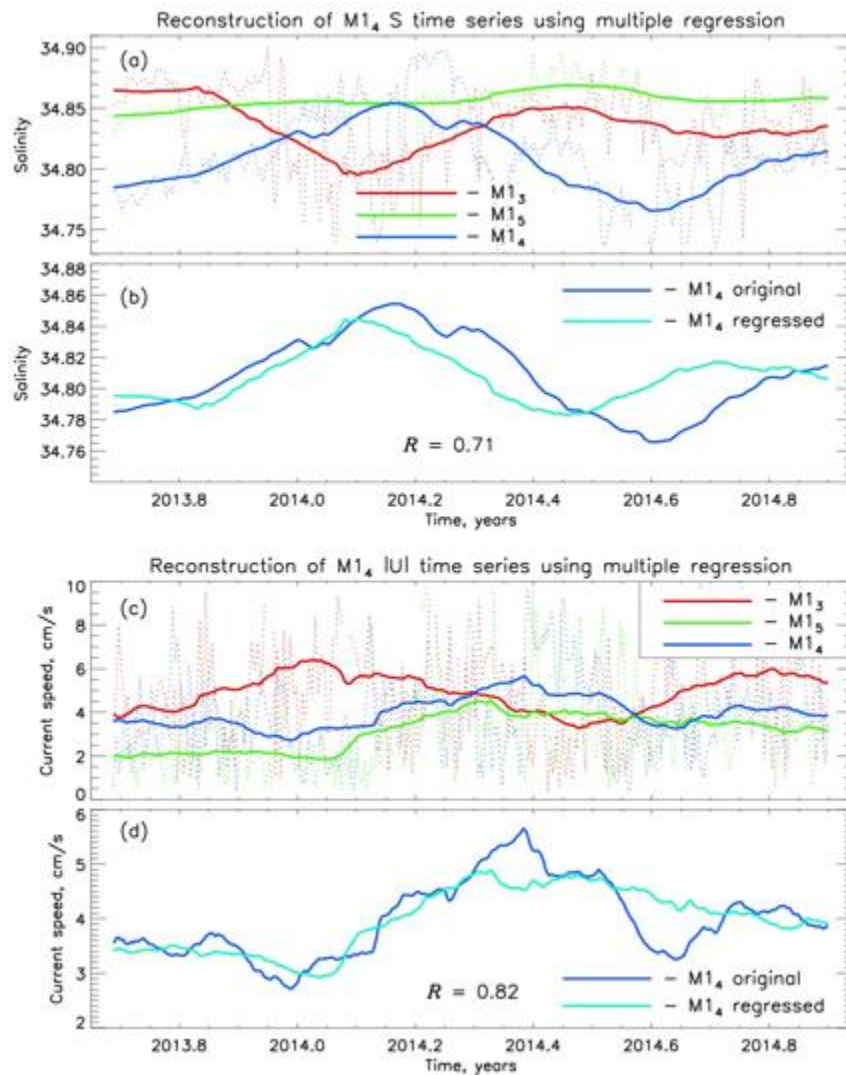
754

755 **Figure 11:** Conceptual model of shift of the mixing regime in the eastern EB in recent years and
 756 associated suite of processes and state conditions including: 1) thinner, more mobile ice, 2)
 757 warmer surface mixed layer (SML), 3) weakening / retreat of cold halocline (HC) layer, 4)
 758 increased AW vertical heat flux (red arrows) and horizontal currents and their vertical shear
 759 (blue arrows), 5) shoaling of upper AW boundary, and 6) replacement of DD by shear
 760 instabilities as the fundamental mechanism of vertical flux.



761

762 **Figure A1:** 2013/15 mean estimates of (top) squared Brunt-Väisälä frequency N^2 , and current
 763 speed $|U|$ for (middle) 20-60 m and (bottom) 190-230 m depth ranges where the mooring records
 764 from M1₃, M1₄, and M1₅ overlap. Statistical significance of estimates for means is shown at the
 765 95% confidence level.



766

767 **Figure A2:** Multiple regression reconstruction of (a,b) salinity and (c,d) current speed $|U|$ at $M1_4$
 768 mooring site using data from $M1_3$ and $M1_5$ moorings for 170-210m depth range. (a,c) Daily
 769 (dotted) and three-month running mean smoothed time series of (a) salinity and (c) $|U|$ from $M1_3$,
 770 $M1_4$, and $M1_5$ moorings. (b,d) Original (blue) and reconstructed (red) time series of (b) salinity
 771 and (d) $|U|$ from $M1_4$ mooring. Relatively high correlations between the original and
 772 reconstructed time series attests of good quality of reconstruction.

773

Table 1: Summary of deep-water moorings used in this study (only those instruments are shown which records have been used here). For mooring locations, see **Fig. 2**.

Mooring	Latitude (N) Longitude (E)	Depth (m)	Instrument	Depth range (m)	Beginning of record	End of record
<i>Moorings deployed in 2002/09 and collocated with M1₄ mooring</i>						
M1a	78 27.360 125 40.440	2680	MMP SBE37	164 – 2598 57, 136	09/02/2002	09/01/2003
M1b	78 26.637 125 40.194	2686	MMP	104 – 1484	09/08/2003	09/09/2004
M1c	78 26.637 125 40.194	2690	ADCP MMP	5 – 50 72 – 900	09/14/2004 09/15/2004	09/15/2005 07/16/2005
M1e	78 25.940 125 43.419	2692	ADCP MMP	5 – 57 70 – 900	09/02/2006	09/18/2007 10/11/2006
M1g	78 25.735 125 28.527	2765	ADCP SBE37	20 – 130 110, 116, 132, 339	10/18/2008 10/19/2008	06/16/2010 09/22/2011
<i>Mooring section M1₁ – M1₆, 2013/15</i>						
M1 ₁	77 04.252 125 48.288	250	ADCP	20 – 250	08/26/2013	09/10/2015
M1 ₂	77 10.376 125 47.516	787	ADCP MMP	5 – 63 70 – 754	10/27/2013 08/26/2013	09/01/2015 08/31/2015
M1 ₃	77 39.286 125 48.401	1849	ADCP MMP	5 – 56 64 – 750	09/06/2013 09/07/2013	09/02/2015 09/03/2015
M1 ₄	78 27.543 125 53.758	2721	ADCP ADCP SBE37	5 – 55 193 – 463 62, 129, 214, 265, 617	09/05/2013	09/19/2015
M1 ₅	80 00.199 125 59.673	3443	ADCP MMP	23 – 83 88 – 754	08/28/2013	06/16/2014 08/21/2015
M1 ₆	81 08.182 125 42.673	3900	ADCP MMP	5 – 55 60 – 754	08/29/2013	09/04/2015 08/22/2015
<i>Mooring section M1₁ – M1₅, 2015/18</i>						
M1 ₁	77 04.221 125 49.577	252	ADCP	200 – 232	09/21/2015	09/03/2018
M1 ₂	77 10.373 125 47.974	783	ADCP SBE	5 – 60 31, 44, 67, 138, 213, 266, 628	09/21/2015	09/03/2018
M1 ₃	77 39.234 125 48.686	1866	ADCP MMP	5 – 55 70 – 1056	09/21/2015 09/22/2015	09/03/2018 06/15/2017
M1 ₄	78 28.084 125 57.679	2700	ADCP ADCP SBE37	5 – 30 155 – 430 38, 107, 188, 240, 604	09/21/2015	09/18/2018
M1 ₅	79 56.194 126 01.228	3443	ADCP MMP	5 – 61 172 – 806	09/21/2015 09/24/2015	08/31/2018 08/29/2018

<i>Mooring M1_{4-short} (September 2 –20, 2018)</i>						
M1 _{4-short}	78 30.833 125 58.924	2700	MMP	30 – 194	09/02/2018	09/20/2018
<i>Moorings M3</i>						
M3e	79 56.136 142 14.887	1335	ADCP SBE	5 – 61 41, 45, 57, 64, 130, 270 600	08/31/2013	09/07/2015
M3f	79 56.194 142 15.216	1357	ADCP SBE	5 – 44 30, 50, 133, 217, 268, 614	09/07/2015	09/06/2018

776
777